Research in Astron. Astrophys. **2012** Vol. **12** No. **10**, 1381–1401
http://www.raa-journal.org *http://www.iop.org/journals/raa*

Research in Astronomy and Astrophysics

Multicolor photometry of the nearby galaxy cluster A119 *

Jin-Tao Tian[1,2,3], Qi-Rong Yuan[4], Xu Zhou[1,3], Zhao-Ji Jiang[1,3], Jun Ma[1,3], Jiang-Hua Wu[5], Zhen-Yu Wu[1,3], Zhou Fan[1,3], Tian-Meng Zhang[1,3] and Hu Zou[1,3]

[1] National Astronomical Observatories, Chinese Academy of Sciences, Beijing 100012, China; *tianjintao2010@gmail.com*
[2] Graduate University of Chinese Academy of Sciences, Beijing 100049, China
[3] Key Laboratory of Optical Astronomy, National Astronomical Observatories, Chinese Academy of Sciences, Beijing 100012, China
[4] Department of Physics, Nanjing Normal University, Nanjing 210046, China
[5] Department of Astronomy, Beijing Normal University, Beijing 100875, China

Received 2011 October 10; accepted 2012 March 31

Abstract This paper presents multicolor optical photometry of the nearby galaxy cluster Abell 119 ($z = 0.0442$) with the Beijing-Arizona-Taiwan-Connecticut system of 15 intermediate bands. Within the BATC field of view of $58' \times 58'$, there are 368 galaxies with known spectroscopic redshifts, including 238 member galaxies (called sample I). Based on the spectral energy distributions of 1376 galaxies brighter than $i_{\rm BATC} = 19.5$, the photometric redshift technique and the color-magnitude relation of early-type galaxies are applied to select faint member galaxies. As a result, 117 faint galaxies were selected as new member galaxies. Combined with sample I, an enlarged sample (called sample II) of 355 member galaxies is obtained. Spatial distribution and localized velocity structure for two samples demonstrate that A119 is a dynamically complex cluster with at least three prominent substructures in the central region within 1 Mpc. A large velocity dispersion for the central clump indicates a merging along the line of sight. No significant evidence for morphology or luminosity segregations is found in either sample. With the PEGASE evolutionary synthesis model, the environmental effect on the properties of star formation is confirmed. Faint galaxies in the low-density region tend to have longer time scales of star formation, smaller mean stellar ages, and lower metallicities in their interstellar medium, which is in agreement with the context of the hierarchical cosmological scenario.

Key words: galaxies: clusters: individual (A119) — galaxies: distances and redshifts — galaxies: evolution — galaxies: kinematics and dynamics — methods: data analysis

1 INTRODUCTION

As the most massive gravitationally bound structures in the universe, clusters of galaxies are not only powerful probes for tracing the large scale structure, but also unique astrophysical laboratories for investigating the evolution of galaxies and dark matter in a dense environment (Bahcall 1988; Pearce

* Supported by the National Natural Science Foundation of China.

et al. 2000; Cortese et al. 2004; Mantz et al. 2008). The hierarchical formation scenario predicts that galaxy clusters are formed by continuous accreting subunits of smaller mass at the nodes of large-scale filaments (West et al. 1991; Katz & White 1993). Substructures in galaxy clusters have been intensively studied since the ROSAT era using the X-ray surface brightness distribution from observations and simulations (Jones & Forman 1984; Ventimiglia et al. 2008; Piffaretti & Valdarnini 2008; Zhang et al. 2009). Based on quantitative measurement of the substructure in nearby clusters, a significant fraction ($> 50\%$) of clusters shows evidence of merging (Geller & Beers 1982; Dressler & Shectman 1988; Mohr et al. 1995; Buote & Tsai 1996), indicating that galaxy clusters are still dynamically young units, undergoing the process of formation (Dressler & Shectman 1988; O'Hara et al. 2006).

The Beijing-Arizona-Taiwan-Connecticut (BATC) galaxy cluster survey aims at obtaining the spectral energy distributions (SEDs) of galaxies in more than 30 nearby clusters in different dynamic states, with 15 intermediate-band filters in the optical band (Yuan et al. 2001). The photometric redshift technique makes it possible to pick up faint cluster galaxies down to $V \sim 20$ mag. With the enlarged sample of member galaxies, dynamical substructures, luminosity function, luminosity segregation and star formation properties of these nearby clusters can be addressed (Yuan et al. 2003; Yang et al. 2004; Zhang et al. 2010; Liu et al. 2011; Pan et al. 2012). As one of the brightest extended X-ray sources with multiple clumps, the galaxy cluster Abell 119 (hereafter A119) is included in the target list of the BATC cluster survey.

The nearby ($z = 0.0442$) cluster A119, located at $00^{\rm h}56^{\rm m}21.4^{\rm s}$, $-01^\circ15'47.0''$(J2000.0), is of richness class 1 (Abell 1958), and is classified as Bautz-Morgan class II – III (Bautz & Morgan 1970). The most luminous member galaxy, UGC 579, is classified as a cD galaxy (Postman & Lauer 1995; Saglia et al. 1997). Peres et al. (1998) argued that there is no cooling flow in this cluster. The reason why A119 appeals to people is its high X-ray luminosity and multiple substructures. Edge et al. (1990) derived a luminosity of $L_{2-10\,\rm keV} \sim 2.58 \times 10^{44}$ erg s^{-1} for A119. Fabricant et al. (1993) argued that substructures in its core show at least three clumps from inspection of X-ray maps and galaxy isopleths. However, Girardi et al. (1997) argued that A119 is a regularly shaped cluster, and no evidence of substructure is found on the basis of their own detection method. There are three discrete radio galaxies in A119, namely 0053–015, 0053–016 and 3C 29 (Feretti et al. 1999). There is no evidence for luminosity segregation in A119 (Pracy et al. 2005).

Figure 1 shows the ROSAT and NVSS smoothed contours superimposed on the $f_{\rm BATC}$-band image of $58' \times 58'$ centered on the cD galaxy UGC 579. The X-ray brightness contour shows a clear NE elongation in the central region, suggesting that A119 is not likely to be a well-relaxed regular cluster.

The structure of this paper is as follows. In Section 2 we describe the BATC multicolor photometric observations and data reduction. In Section 3, spatial distribution and dynamics of cluster galaxies with known spectroscopic redshifts are investigated. The photometric redshift technique and its application in the selection of faint member galaxies are described in Section 4. In Section 5, based on an enlarged sample of cluster galaxies, we unveil some observational properties of A119, such as spatial distribution, dynamics, morphology-density relation and luminosity segregation. In Section 6, star formation properties for the spectroscopically-confirmed member galaxies are presented. Finally, we summarize our work in Section 7. Throughout this paper, the ΛCDM cosmology model with H_0=73 km s^{-1} Mpc^{-1}, $\Omega_m = 0.3$ and $\Omega_\Lambda = 0.7$ is assumed.

2 OBSERVATIONS AND DATA REDUCTION

The observations of A119 were carried out with the 60/90 cm f/3 Schmidt Telescope of National Astronomical Observatories of China (NAOC), at the Xinglong station at an altitude of 900 m. The BATC multicolor photometric system includes 15 intermediate-band filters, namely $a-k$ and $m-p$, covering the whole optical wavelength range from about 3000 to 10 000 Å. These filters are specially

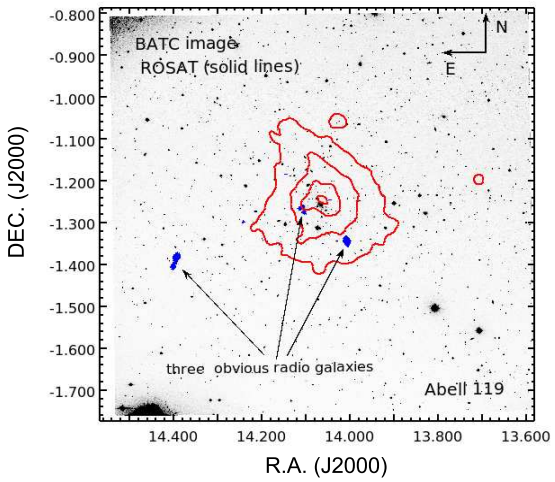

Fig. 1 The smoothed contours of the ROSAT PSPC image in the soft X-ray band (0.1–2.4 keV) (*solid lines*) and the NVSS FIRST (Faint Images of the Radio Sky at Twenty-cm) map at a wavelength of 20 cm, overlaying on an optical image of $58' \times 58'$ in the BATC f band. The sizes of Gaussian smoothing windows are adopted as $30''$ and $4'$ for the radio and X-ray contours, respectively.

designed to avoid most bright night-sky emission lines (Yan et al. 2000). The transmission curves can be seen in Yuan et al. (2003).

A 2048 $\times$ 2048 Ford CCD camera was equipped with the BATC system before 2006 October. The field of view was $58' \times 58'$, with a scale of $1.7''$ per pixel. For pursuing better spatial resolution and higher sensitivity in blue bands, a new E2V 4096 $\times$ 4096 CCD has now been put into service. This CCD has a quantum efficiency of 92.2% at 4000 Å and the field of view is extended to $92' \times 92'$. The spatial scale becomes $1.36''$per pixel since the pixel size is 12 μm, exactly 4/5 of the former pixel size (15 μm). The details of the telescope, camera and data-acquisition system can be found in Zhou et al. (2001); Yan et al. (2000).

From 2002 September to 2006 November, only 12 BATC filters, from *d* to *p*, were applied to the target A119 with the old CCD, forming a discontinuous series. Since 2007, the exposures in the *a*, *b* and *c* bands have been completed with a new CCD camera. In total, we have about 54 hr of exposure (see more details in Table 1).

The standard procedures of bias substraction, dome flat-field correction and position calibration were carried out with automatic data-processing software, PIPLINE I, developed specially for BATC multicolor photometry (Fan et al. 1996; Zhou et al. 2001). The cosmic rays and bad pixels were corrected by comparing multiple images in sequential combinations.

For detecting sources and measuring the fluxes within a given aperture in the combined BATC images, we use the photometry package PIPELINE II, developed on the basis of the DAOPHOT (Stetson 1987) kernel (Zhou et al. 2003a). The objects with a signal-to-noise ratio greater than the threshold 3.5σ in the i, j and k bands are considered to be detected. Because the pixel size ratio between the old and new CCDs is 5:4, an aperture radius of 4 pixels (i.e. $r = 1.7'' \times 4 = 6.8''$) is taken for the images in 12 redder bands (d to p), and a radius of 5 pixels ($r = 1.36'' \times 5 = 6.8''$) is adopted for the images in bluer bands (*a*,*b*,*c*). Flux calibration in the BATC system is performed by using four Oke-Gunn standard stars (HD 19445, HD 84937, BD+262606 and BD+17 4708) (Gunn & Stryker 1983). The procedures of BATC flux calibration are slightly corrected by Zhou et al. (2001). Model calibration on the basis of the stellar SED library is performed to check the results

Table 1 Parameters of the BATC Filters and the Observational Statistics of A119

No.	Filter Name	$\lambda_{\rm eff}$[a] (Å)	FWHM (Å)	Exposure (s)	Number of Images	Seeing[b] (arcsec)	Completeness Magnitude	Objects Detected
1	a	3371	356	20760	19	4.18	21.0	7526
2	b	3894	294	4860	12	5.94	20.5	7471
3	c	4201	297	8880	11	4.36	20.5	7959
4	d	4546	367	24000	23	4.15	20.5	6079
5	e	4872	377	19800	19	4.95	20.5	7745
6	f	5247	338	12000	13	4.50	20.5	6813
7	g	5784	285	8400	10	3.51	20.0	7400
8	h	6073	310	8100	9	3.48	19.5	7730
9	i	6709	518	3960	5	3.65	19.5	8158
10	j	7010	168	6900	8	4.11	19.0	7254
11	k	7526	200	8400	10	3.78	19.0	6711
12	m	8024	256	15900	17	3.98	19.0	7250
13	n	8517	160	12000	13	4.77	19.0	7879
14	o	9173	255	25200	24	4.15	18.5	8219
15	p	9723	280	22079	22	4.25	18.5	7158

[a] Effective wavelengths of the filters; [b] This column lists the seeing of the combined images.

of flux calibration via standard stars (Zhou et al. 1999). The flux measurements derived by these two calibration methods are in accordance with each other for most filters. As a result, the SEDs of 10 605 sources have been obtained.

Spatial scale at cluster redshift $z = 0.0442$ is 0.834 kpc arcsec^{-1}. The typical seeing of combined images in the BATC bands is about 4.2″, corresponding to 3.5 kpc, which is smaller than the size of a typical spiral galaxy. For checking the completeness of the BATC detection of galaxies, we compare the SDSS galaxies down to $r < 19.5$ within a central region with a radius of 0.5 degree. There are 1121 SDSS-detected galaxies, among which 1017 galaxies are also detected by the BATC photometry, corresponding to a completeness of 90.7%.

3 ANALYSIS OF CLUSTER GALAXIES WITH KNOWN SPECTROSCOPIC REDSHIFTS

3.1 Sample of Spectroscopically-Confirmed Member Galaxies

For investigating the properties of galaxy cluster A119, 368 normal galaxies with known spectroscopic redshifts ($z_{\rm sp}$) are extracted in our field of view from the NASA/IPAC Extragalactic Database (NED). We cross-identified all these galaxies with the BATC-detected sources.

In order to eliminate foreground and background galaxies, we apply a standard iterative 3σ-clipping algorithm (Yahil & Vidal 1977) to the velocity distribution. For a galaxy cluster with complex dynamics, the velocity distribution is expected to be non-Gaussian. Using the ROSTAT software, we can derive two resistant and robust estimators, the biweight location ($C_{\rm BI}$) and scale ($S_{\rm BI}$), analogous to the velocity mean and dispersion (Beers et al. 1990). The galaxies with velocities between ($C_{\rm BI} - 3S_{\rm BI}$) and ($C_{\rm BI} + 3S_{\rm BI}$) are selected as member galaxies. After reaching convergence, we achieve $C_{\rm BI} = 13\,298^{+93}_{-96}$ km s^{-1} and $S_{\rm BI} = 854^{+80}_{-65}$ km s^{-1}. The errors of these two estimators correspond to the 90% confidence interval, and they are calculated by bootstrap resamplings of 10 000 subsamples of the velocity data. There are 238 member galaxies with 10 736 km s^{-1} $< cz <$ 15 860 km s^{-1}, and we refer to these galaxies as "sample I." Based on 153 member galaxies of A119, Way et al. (1997) derived $C_{\rm BI} = 13\,228^{+103}_{-98}$ km s^{-1} and $S_{\rm BI} = 778^{+122}_{-88}$ km s^{-1}, slightly smaller than our estimation. Fabricant et al. (1993) derived a mean radial velocity of $13\,293 \pm 101$ km s^{-1} and a velocity dispersion of 857^{+78}_{-61} km s^{-1} based on 80 member galaxies, which is in good agreement with our statistics.

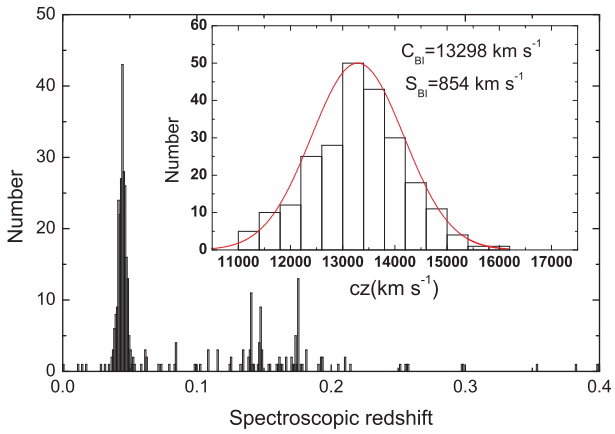

Fig. 2 The histogram of spectroscopic redshifts between 0.0 and 0.4 for 368 galaxies detected by all multicolor surveys. The embedded panel shows the histogram of the radial velocity (cz) distribution of 238 galaxies in A119 in bins of 400 $\mathrm{km\ s^{-1}}$.

Figure 2 shows the distribution of spectroscopic redshifts for those 368 galaxies. We take the NED-given cluster redshift of $\bar{z}_c = 0.0442$ for A119. For testing normality of the velocity distribution, we apply the Shapiro-Wilk W test to sample I, and obtain the statistic $W = 0.995$, corresponding to a probability value of $P = 0.648$ which is much greater than the critical value $P = 0.05$. This indicates that the velocity distribution for sample I is consistent with a Gaussian. The embedded panel of Figure 2 shows the histogram of radial velocities with a Gaussian fit. With the velocities and positions of these member galaxies, the mass of A119 can be derived by applying the virial theorem, assuming this cluster is well virialized (Geller & Peebles 1973; Oegerle & Hill 1994). We obtain a virial mass of $8.86 \times 10^{14} M_{\odot}$.

Table 2 lists the spectroscopic redshifts of 238 member galaxies in sample I.

3.2 Spatial Distribution and Localized Velocity Structure

A contour map of galaxy surface number density is an intuitive tool for finding the existence of substructures in galaxy clusters. The left panel of Figure 3 shows contour maps of surface density with a Gaussian smoothing window of $\sigma = 2'$ superimposed on the projected positions of 238 galaxies in sample I. As shown by the contour map, A119 does not appear to be spherically asymmetric, and at least three clumps can be found. It seems to agree with the X-ray brightness map (see Fig. 1), which indicates the presence of substructures in A119.

The spatial distribution of clumps might be due to the effect of projection. For eliminating the ambiguity in substructure detection, we apply the κ-test to sample I for quantifying the localized variation in a velocity distribution. The statistic κ_n is introduced by Colless & Dunn (1996) to quantify the local deviation on the scale of n nearest neighbors

$$\kappa_n = \sum_{i=1}^{N} -\log[P_{\mathrm{KS}}(D > D_{\mathrm{obs}})],$$

where N is the number of member galaxies, and $[P_{\mathrm{KS}}(D > D_{\mathrm{obs}})]$ represents the probability of the standard Kolmogorov-Smirnov (K-S) statistic D being greater than the observed value D_{obs}. Thus a greater κ_n means a greater probability that the local velocity distribution differs from the

Table 2 Catalog of 238 Spectroscopically Confirmed Member Galaxies in A119

No.	R.A. (h m s)	Dec. (° ′ ″)	$z_{\rm sp}$	Ref.	No.	R.A. (h m s)	Dec. (° ′ ″)	$z_{\rm sp}$	Ref.
1	00 56 21.0	−01 13 33	0.036755	[1]	60	00 56 27.6	−01 23 15	0.042379	[1]
2	00 56 18.4	−01 08 04	0.036889	[2]	61	00 56 16.2	−01 18 50	0.042416	[1]
3	00 56 24.7	−01 16 42	0.037232	[1]	62	00 56 42.8	−01 13 26	0.042429	[1]
4	00 56 11.1	−01 19 42	0.037489	[1]	63	00 56 20.3	−01 14 33	0.042476	[1]
5	00 56 12.9	−01 15 48	0.037783	[1]	64	00 56 07.0	−01 28 28	0.042499	[1]
6	00 56 25.6	−01 15 45	0.038223	[3]	65	00 56 01.9	−01 32 59	0.042563	[2]
7	00 56 29.2	−01 13 36	0.038403	[1]	66	00 55 54.4	−01 03 50	0.042586	[1]
8	00 56 17.9	−01 15 43	0.038580	[1]	67	00 55 50.7	−01 11 20	0.042613	[1]
9	00 55 51.5	−01 14 04	0.038588	[4]	68	00 56 02.7	−01 20 04	0.042689	[3]
10	00 56 32.4	−01 11 15	0.038677	[2]	69	00 55 30.5	−01 24 51	0.042763	[2]
11	00 57 03.0	−01 20 42	0.038680	[1]	70	00 55 31.1	−01 13 24	0.042793	[8]
12	00 56 21.0	−01 10 36	0.039130	[2]	71	00 55 39.9	−01 29 21	0.042806	[1]
13	00 56 17.8	−01 15 37	0.039154	[2]	72	00 56 56.5	−00 56 37	0.042836	[2]
14	00 57 13.7	−01 00 44	0.039230	[2]	73	00 56 17.1	−01 23 07	0.042840	[2]
15	00 56 18.0	−01 16 22	0.039254	[1]	74	00 56 39.7	−01 28 29	0.042863	[2]
16	00 54 42.1	−01 29 22	0.039561	[5]	75	00 55 45.9	−01 12 27	0.043023	[1]
17	00 55 28.5	−01 19 25	0.039747	[1]	76	00 57 48.7	−01 00 15	0.043090	[2]
18	00 55 29.5	−01 07 58	0.039771	[2]	77	00 56 06.0	−01 03 26	0.043123	[2]
19	00 55 46.8	−01 17 08	0.039948	[1]	78	00 57 51.7	−01 08 10	0.043143	[4]
20	00 56 26.1	−01 09 25	0.040011	[1]	79	00 55 47.8	−01 42 10	0.043223	[2]
21	00 54 38.7	−01 10 11	0.040066	[4]	80	00 55 05.0	−01 15 09	0.043313	[2]
22	00 57 09.7	−01 22 49	0.040188	[2]	81	00 57 14.6	−01 17 09	0.043370	[2]
23	00 55 38.2	−01 11 00	0.040355	[1]	82	00 55 40.7	−01 18 44	0.043423	[3]
24	00 56 46.0	−01 32 39	0.040365	[2]	83	00 57 26.3	−01 20 37	0.043450	[2]
25	00 56 18.6	−01 13 07	0.040365	[1]	84	00 56 57.0	−01 23 20	0.043497	[2]
26	00 56 39.3	−01 04 37	0.040441	[1]	85	00 56 04.0	−01 13 03	0.043543	[4]
27	00 55 16.2	−01 30 50	0.040581	[2]	86	00 55 27.0	−01 13 23	0.043544	[4]
28	00 55 55.6	−01 14 50	0.040778	[2]	87	00 56 25.9	−01 16 30	0.043583	[2]
29	00 56 51.5	−01 16 21	0.041002	[2]	88	00 57 59.9	−01 25 09	0.043607	[5]
30	00 56 02.3	−01 29 46	0.041058	[1]	89	00 56 47.1	−00 52 41	0.043617	[2]
31	00 55 35.6	−01 14 08	0.041116	[4]	90	00 56 18.1	−01 14 31	0.043647	[2]
32	00 55 57.2	−01 30 50	0.041182	[1]	91	00 54 29.8	−01 10 17	0.043655	[4]
33	00 55 51.2	−00 48 50	0.041194	[4]	92	00 56 45.3	−00 56 27	0.043658	[4]
34	00 55 32.9	−01 11 33	0.041205	[1]	93	00 56 19.7	−01 17 10	0.043727	[1]
35	00 56 13.6	−01 13 38	0.041235	[1]	94	00 56 47.1	−01 16 57	0.043800	[1]
36	00 55 42.0	−01 03 31	0.041235	[1]	95	00 56 12.8	−00 50 02	0.043805	[4]
37	00 57 10.7	−01 01 08	0.041298	[2]	96	00 56 37.2	−01 32 24	0.043817	[1]
38	00 55 21.4	−01 21 08	0.041472	[2]	97	00 56 32.2	−01 21 04	0.043847	[1]
39	00 55 55.0	−01 02 59	0.041569	[1]	98	00 56 16.4	−01 32 36	0.043897	[2]
40	00 56 20.3	−01 15 02	0.041575	[1]	99	00 57 11.6	−01 37 11	0.043934	[8]
41	00 55 25.2	−01 18 32	0.041585	[2]	100	00 56 27.4	−00 47 33	0.043940	[2]
42	00 56 37.8	−01 20 41	0.041589	[1]	101	00 55 52.2	−01 30 06	0.043957	[2]
43	00 54 41.0	−01 34 29	0.041625	[6]	102	00 56 29.3	−01 20 25	0.044034	[2]
44	00 55 44.9	−01 12 57	0.041649	[4]	103	00 56 41.6	−01 19 33	0.044080	[1]
45	00 56 47.4	−00 55 12	0.041686	[4]	104	00 55 45.6	−01 03 17	0.044110	[1]
46	00 55 22.9	−01 12 40	0.041782	[2]	105	00 56 38.5	−01 23 26	0.044117	[2]
47	00 55 39.0	−01 25 15	0.041842	[1]	106	00 56 23.5	−00 59 13	0.044137	[2]
48	00 57 53.7	−00 48 53	0.041849	[6]	107	00 55 16.9	−00 55 05	0.044179	[4]
49	00 56 10.7	−01 07 01	0.041856	[2]	108	00 55 38.2	−01 16 46	0.044197	[1]
50	00 55 47.2	−01 13 53	0.041876	[1]	109	00 57 02.0	−00 52 31	0.044238	[4]
51	00 56 22.2	−01 06 43	0.041956	[1]	110	00 55 54.2	−00 55 21	0.044264	[9]
52	00 56 38.2	−01 17 53	0.041972	[1]	111	00 55 12.9	−01 19 18	0.044274	[2]
53	00 56 46.4	−01 16 51	0.042060	[7]	112	00 56 40.9	−01 02 04	0.044277	[2]
54	00 55 45.6	−01 05 03	0.042139	[4]	113	00 56 01.7	−01 03 52	0.044284	[8]
55	00 54 38.8	−01 34 27	0.042216	[6]	114	00 55 16.4	−01 21 05	0.044291	[1]
56	00 55 43.2	−01 02 01	0.042266	[2]	115	00 56 35.7	−01 15 56	0.044354	[1]
57	00 56 30.7	−01 10 22	0.042273	[2]	116	00 55 53.6	−00 54 04	0.044357	[2]
58	00 54 26.1	−00 55 42	0.042321	[4]	117	00 55 05.5	−01 14 02	0.044407	[2]
59	00 56 31.5	−01 21 42	0.042359	[2]	118	00 56 58.5	−01 15 25	0.044434	[2]

Table 2 — *Continued.*

No.	R.A. (h m s)	Dec. (° ′ ″)	$z_{\rm sp}$	Ref.	No.	R.A. (h m s)	Dec. (° ′ ″)	$z_{\rm sp}$	Ref.
119	00 55 51.2	−01 18 23	0.044444	[8]	179	00 55 19.1	−01 11 16	0.046149	[1]
120	00 56 16.1	−01 15 19	0.044464	[3]	180	00 56 15.8	−01 26 48	0.046182	[1]
121	00 56 03.3	−00 49 41	0.044464	[2]	181	00 56 21.8	−01 26 58	0.046205	[2]
122	00 58 02.1	−00 49 37	0.044503	[4]	182	00 55 16.3	−01 24 16	0.046232	[1]
123	00 57 08.5	−01 29 39	0.044591	[8]	183	00 56 07.1	−01 20 36	0.046272	[6]
124	00 55 57.9	−01 14 24	0.044597	[4]	184	00 54 50.6	−01 28 45	0.046295	[2]
125	00 56 39.6	−01 04 43	0.044602	[4]	185	00 56 25.1	−01 18 37	0.046299	[1]
126	00 55 59.6	−01 32 09	0.044624	[1]	186	00 54 54.6	−01 20 27	0.046305	[1]
127	00 56 38.7	−01 21 06	0.044627	[1]	187	00 56 56.7	−01 27 11	0.046319	[1]
128	00 56 00.0	−01 16 16	0.044637	[1]	188	00 56 07.8	−01 25 47	0.046365	[1]
129	00 56 12.8	−01 16 10	0.044671	[2]	189	00 56 25.6	−01 30 41	0.046432	[1]
130	00 55 55.1	−01 03 51	0.044694	[2]	190	00 57 03.0	−00 52 25	0.046472	[2]
131	00 55 49.6	−01 04 54	0.044716	[4]	191	00 56 27.7	−01 01 27	0.046525	[2]
132	00 56 18.1	−01 37 33	0.044771	[2]	192	00 56 41.0	−01 18 26	0.046542	[1]
133	00 55 40.8	−00 59 50	0.044779	[4]	193	00 57 02.0	−00 52 47	0.046585	[6]
134	00 57 07.8	−01 27 54	0.044781	[8]	194	00 56 26.6	−01 20 53	0.046615	[1]
135	00 56 31.4	−01 36 59	0.044801	[2]	195	00 55 03.6	−01 19 03	0.046689	[1]
136	00 55 51.6	−01 30 23	0.044814	[1]	196	00 56 18.8	−01 28 12	0.046812	[1]
137	00 56 04.9	−01 08 09	0.044830	[4]	197	00 56 44.5	−00 52 29	0.046842	[2]
138	00 56 53.2	−01 17 42	0.044858	[1]	198	00 54 49.4	−01 23 19	0.046972	[1]
139	00 55 18.8	−01 16 38	0.044888	[3]	199	00 56 17.6	−01 17 43	0.047176	[1]
140	00 56 39.3	−01 34 39	0.044931	[8]	200	00 57 41.6	−01 18 44	0.047186	[6]
141	00 57 04.9	−00 55 09	0.044951	[2]	201	00 55 58.6	−01 12 10	0.047206	[1]
142	00 56 14.3	−01 08 40	0.044961	[2]	202	00 54 53.4	−01 34 35	0.047266	[2]
143	00 55 54.5	−00 55 14	0.044964	[2]	203	00 56 11.2	−01 07 40	0.047299	[1]
144	00 55 57.3	−01 22 15	0.044971	[1]	204	00 56 11.3	−01 31 35	0.047373	[1]
145	00 55 45.4	−01 23 59	0.045008	[2]	205	00 55 18.5	−01 19 05	0.047549	[1]
146	00 57 34.9	−01 23 28	0.045031	[3]	206	00 57 15.5	−00 49 31	0.047688	[4]
147	00 56 27.9	−01 26 07	0.045061	[2]	207	00 56 33.7	−01 09 52	0.047746	[1]
148	00 56 23.0	−01 14 58	0.045118	[1]	208	00 55 13.6	−01 04 34	0.047773	[2]
149	00 57 31.8	−00 55 40	0.045154	[2]	209	00 56 51.6	−01 00 26	0.047796	[4]
150	00 56 00.7	−01 27 03	0.045181	[1]	210	00 55 51.1	−01 09 53	0.047810	[2]
151	00 56 46.6	−01 35 47	0.045211	[5]	211	00 56 52.7	−01 07 53	0.047880	[4]
152	00 56 13.3	−01 16 12	0.045318	[2]	212	00 56 30.0	−01 05 13	0.047916	[4]
153	00 56 38.4	−01 07 34	0.045358	[2]	213	00 56 15.0	−01 15 47	0.047936	[1]
154	00 55 55.0	−01 14 49	0.045368	[1]	214	00 55 39.7	−00 52 36	0.047954	[4]
155	00 57 22.7	−00 49 19	0.045376	[4]	215	00 56 57.8	−01 09 29	0.048092	[4]
156	00 55 17.9	−01 17 11	0.045421	[2]	216	00 56 30.4	−01 32 02	0.048167	[2]
157	00 55 03.2	−01 15 57	0.045508	[2]	217	00 56 26.8	−01 19 48	0.048383	[1]
158	00 55 53.3	−01 06 59	0.045520	[4]	218	00 56 10.4	−01 08 25	0.048393	[2]
159	00 55 11.2	−00 48 37	0.045623	[4]	219	00 56 11.9	−01 16 39	0.048523	[1]
160	00 56 16.2	−01 09 46	0.045635	[1]	220	00 55 43.7	−01 19 46	0.048614	[1]
161	00 55 08.9	−01 02 47	0.045655	[2]	221	00 56 13.4	−01 14 18	0.048662	[4]
162	00 56 15.4	−01 05 54	0.045748	[1]	222	00 57 06.9	−01 23 51	0.048707	[2]
163	00 55 45.3	−01 19 28	0.045755	[2]	223	00 55 19.2	−01 31 01	0.048707	[1]
164	00 56 26.5	−01 37 34	0.045765	[2]	224	00 57 11.1	−01 22 49	0.048827	[6]
165	00 57 39.8	−00 53 33	0.045789	[4]	225	00 57 00.3	−00 49 31	0.048850	[2]
166	00 56 52.7	−01 09 33	0.045812	[2]	226	00 56 11.3	−01 31 53	0.048947	[2]
167	00 55 08.8	−01 23 48	0.045825	[8]	227	00 55 59.1	−01 18 01	0.048977	[2]
168	00 56 10.2	−01 16 04	0.045838	[2]	228	00 55 38.2	−01 34 47	0.049030	[6]
169	00 55 25.8	−01 23 02	0.045908	[1]	229	00 56 58.3	−01 22 45	0.049101	[1]
170	00 56 43.2	−01 23 45	0.045958	[1]	230	00 56 48.7	−01 29 32	0.049564	[1]
171	00 55 32.3	−01 12 40	0.045967	[4]	231	00 56 22.8	−01 12 35	0.049918	[2]
172	00 55 59.2	−01 09 49	0.045993	[4]	232	00 56 56.9	−01 12 43	0.049991	[4]
173	00 56 56.0	−00 59 48	0.046020	[4]	233	00 56 39.0	−01 17 43	0.050155	[5]
174	00 57 06.4	−00 54 31	0.046032	[2]	234	00 55 57.6	−01 17 26	0.050628	[2]
175	00 55 14.7	−00 49 20	0.046037	[4]	235	00 56 39.1	−01 05 23	0.050902	[1]
176	00 55 30.8	−01 17 50	0.046052	[1]	236	00 56 54.2	−01 15 25	0.051325	[1]
177	00 55 42.9	−01 11 46	0.046132	[1]	237	00 56 34.5	−01 16 49	0.052399	[1]
178	00 56 11.3	−00 58 13	0.046139	[2]	238	00 55 31.2	−01 11 33	0.052850	[1]

References: [1] Cava et al. (2009); [2] Smith et al. (2004); [3] Wegner et al. (1999); [4] Abazajian et al. (2003); [5] Dale et al. (1998); [6] Rines et al. (2003); [7] Kinman & Hintzen (1981); [8] Katgert et al. (1998); [9] Fabricant et al. (1993).

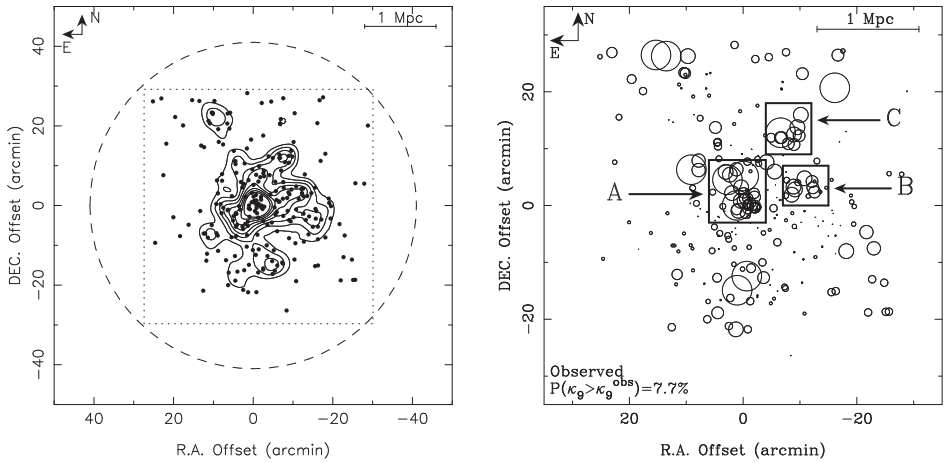

Fig. 3 *Left*: Spatial distribution for 238 spectroscopic member galaxies of A119 in sample I (denoted by filled circles). The contour map of the surface density uses the Gaussian smoothing window $\sigma = 2'$. The contour map is superposed with the surface density levels 0.11, 0.16, 0.21, 0.26, 0.31, 0.36, 0.41 and 0.46 arcmin^{-2}. The large dashed circles show a typical region of rich clusters with a radius of $R \approx 1.5h^{-1}$ Mpc from the cluster center. The region within the dotted line represents the BATC field. *Right*: Bubble plot showing the localized variation for groups of the nine nearest neighbors for 238 member galaxies in sample I.

overall distribution. The probability $P\ (\kappa_n > \kappa_n^{\rm obs})$ can be estimated by Monte Carlo simulations by randomly shuffling velocities.

Table 3 gives the results of the κ-test for samples I and II (sample II will be defined in the next section). For the 238 member galaxies in sample I, the probability $P\ (\kappa_n > \kappa_n^{\rm obs})$ is found to be less than 15% for a range of neighbor sizes ($6 \leq n \leq 12$), indicating the probable presence of substructure in A119.

Table 3 κ-test for Member Galaxies in Samples I and II of A119

Neighbor size n	Sample I $P(\kappa_n > \kappa_n^{\rm obs})$ (%)	Sample II $P(\kappa_n > \kappa_n^{\rm obs})$ (%)
6	14.1	<0.1
7	14.6	<0.1
8	13.9	0.2
9	7.7	0.7
10	8.5	1.1
11	9.4	0.6
12	11.1	0.5

Bubble plots in the case of nine nearest neighbors are shown in the right-hand panel of Figure 3. The bubble size at the position of each galaxy is proportional to $-\log[P_{\rm KS}(D > D_{\rm obs})]$. Consequently, the larger bubbles indicate a greater difference between local and overall velocity distributions. For sample I, three remarkable bubble clumps, called A, B and C, can be found. The southern 'clump' shown in the contour map (see the left panel) is not real, because no bubble clustering appears at the same location. The big bunch of bubbles in the central region obviously indicates an anomalous velocity distribution at the center. For observing the anomalous kinematics in bubble

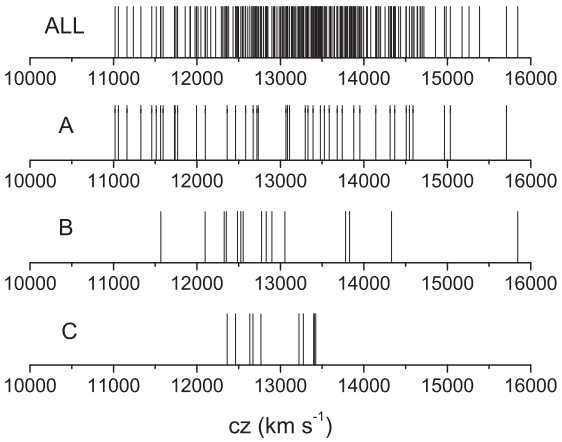

Fig. 4 Stripe density plot of velocity of the spectroscopically confirmed galaxies in the whole cluster, and clumps A, B and C, respectively.

clumps, the stripe densities of velocity distributions are presented in Figure 4. For clumps A and C, their velocity distributions have anomalous dispersions. Compared with the dispersion of overall sample I ($S_{BI} = 854^{+80}_{-65}\ \mathrm{km\,s^{-1}}$), clump A has a very large dispersion ($S_{BI} = 1282^{+205}_{-152}\ \mathrm{km\,s^{-1}}$), while clump C has a significantly smaller dispersion ($S_{BI} = 443^{+110}_{-342}\ \mathrm{km\,s^{-1}}$). Clump B is found to have a smaller mean velocity ($C_{BI} = 12\,733^{+710}_{-261}\ \mathrm{km\,s^{-1}}$). Keep in mind that the errors of the above biweight estimators correspond to a 90% confidence interval. The above biweight estimators in clumps differ from those for the whole sample at more than a 3σ significance level. It is interesting that 85% of the member galaxies with $cz < 11\,500\ \mathrm{km\,s^{-1}}$ are found in clump A, which unambiguously points to a merging along the line-of-sight direction in the cluster core. Clump C seems to be a compact group of galaxies with a bulk velocity of $12\,966\ \mathrm{km\,s^{-1}}$. The classic K-S test shows that the difference for velocity distributions between each clump (A/B/C) and the overall sample I is very significant, corresponding to probabilities of 91.4%, 96% and 95.2%, respectively. This means the three clumps are probably real substructures.

4 PHOTOMETRIC REDSHIFT TECHNIQUE AND SELECTION OF FAINT MEMBERS

4.1 Membership Selection by Photometric Redshift Technique

Although optical spectroscopy is a straightforward approach for the determination of cluster membership, spectroscopy of faint galaxies remains a rather daunting task. The photometric redshift technique plays a crucial role in finding faint galaxies based on their SEDs (Pelló et al. 1999; Brunner & Lubin 2000).

The photometric redshift technique has been applied extensively in deep photometric surveys with large-field detectors (Lanzetta et al. 1996; Arnouts et al. 1999; Furusawa et al. 2000). A standard SED-fitting code, called HYPERZ (Bolzonella et al. 2000), is adopted for estimating the photometric redshifts. The procedure has been specially adapted for the BATC multicolor photometric system (Yuan et al. 2001; Xia et al. 2002; Zhou et al. 2003b). The SED templates for normal galaxies are generated through convolving the galaxy spectra in the GISSEL98 (Galaxy Isochore Synthesis Spectral Evolution Library; Bruzual A. & Charlot 1993) template library with transmission curves of the BATC filters. For a given source, the photometric redshift, z_{ph}, corresponds to the best fit (in

the χ^2-sense) between photometric SED and template SED. The reddening law of the Milky Way (Allen 1976) is adopted for dust extinction, and A_V is flexible in a range from 0.0 to 0.2.

Through cross-identification between the SDSS photometric catalog and the BATC-detected sources, 1376 galaxies in our field of view are extracted, including 1008 faint galaxies without spectroscopic redshifts. As a test, we first let $z_{\rm ph}$ vary in a wide range from 0.0 to 1.0, with steps of 0.01. Only a small number of galaxies are found to have $z_{\rm ph} > 0.4$. We search the photometric redshifts for 1376 galaxies that are brighter than $i_{\rm BATC} = 19.5$ in a range from 0.0 to 0.4, with a step of 0.001.

To evaluate the precision of our $z_{\rm ph}$ estimation, a comparison between $z_{\rm ph}$ and $z_{\rm sp}$ values for galaxies brighter than $i_{\rm BATC} = 17.0$ is given in Figure 5. The dashed lines indicate an average redshift deviation of 0.0103, and error bars of $z_{\rm ph}$ correspond to the 68% confidence level in photometric redshift determination. Our $z_{\rm ph}$ estimates are basically in accordance with the $z_{\rm sp}$ values. In Figure 5, there are five galaxies whose $z_{\rm ph}$ values significantly deviate from the spectroscopic redshifts. We check images and SEDs of these galaxies, and find that the SEDs of some galaxies suffer from some satellite contamination within the aperture, and some galaxies are located at the edge of the BATC field, which result in false SEDs.

An iterative 2σ-clipping algorithm is applied to the $z_{\rm ph}$ values of 238 member galaxies in sample I. We obtain $C_{\rm BI}= 0.048^{+0.01}_{-0.01}$ and $S_{\rm BI} = 0.09^{+0.01}_{-0.01}$ for the $z_{\rm ph}$ estimate. Statistically, 137 of 144 member galaxies (about 95%) brighter than $i_{\rm BATC} = 17.0$ are found to have their photometric redshifts within the $\pm 2S_{\rm BI}$ deviation, corresponding to a $z_{\rm ph}$ range from 0.030 to 0.066. Even for all 238 member galaxies in sample I, 192 galaxies (about 81%) are found to have $0.030 < z_{\rm ph} < 0.066$. The $z_{\rm ph}$ range is taken as a selection criterion of faint member candidates. As a result, 144 galaxies with $0.030 < z_{\rm ph} < 0.066$ are regarded as new member candidates of A119. The distributions of photometric redshift for sample I and new member candidates are shown in Figure 6. The dashed lines denote the $z_{\rm ph}$ range of the selection criterion.

4.2 Color-Magnitude Correlation

A universal correlation between color and absolute magnitude for early-type galaxies, called the CM relation, has commonly been found in rich galaxy clusters (Bower et al. 1992, and references therein). Brighter early-type galaxies tend to be redder. The SDSS photometric catalog provides a parameter, `fracDeV`, defined as a fraction of the brightness contribution by the de Vaucouleurs component. We take the galaxies with `fracDeV` > 0.5 as early-types, and the remaining as late-type galaxies. The CM relation can be used to constrain the membership selection of early-type galaxies (Yuan et al. 2001).

Figure 7 shows the relation between color index $b - h$ and h magnitude for member galaxies in sample I and newly-selected member candidates. A linear fitting is performed for the 181 early-type galaxies in sample I: $b - h = -0.20(\pm 0.01)h + 5.44(\pm 0.19)$, and dashed lines denote a $\pm 3\sigma$ deviation. A majority of early-type member galaxies in sample I follows a tight color-magnitude correlation. However, 27 early-type candidates of member galaxies are scattered beyond the intercept that denotes the 3σ deviation, and they have been removed from our candidate list.

Finally, a list of 355 member galaxies is obtained by combining the 238 spectroscopically confirmed member galaxies in sample I (including 181 early-type galaxies and 57 late-type galaxies) with the 117 newly selected member galaxies (including 36 early-type galaxies and 81 late-type galaxies), to which we refer as sample II. SED information, the SDSS morphological parameter 'fracDeV,' and photometric redshifts for the 117 newly selected member galaxies are cataloged in Table 4. The magnitude of 99.00 means non-detection in the specified band.

For estimating the percentage of object blending due to the seeing effect, a cross-identification of the 117 new candidates of member galaxies is performed with the photometric catalog of the SDSS galaxies. A searching circle with a radius of $4.5''$ centered at BATC-detected galaxies is adopted,

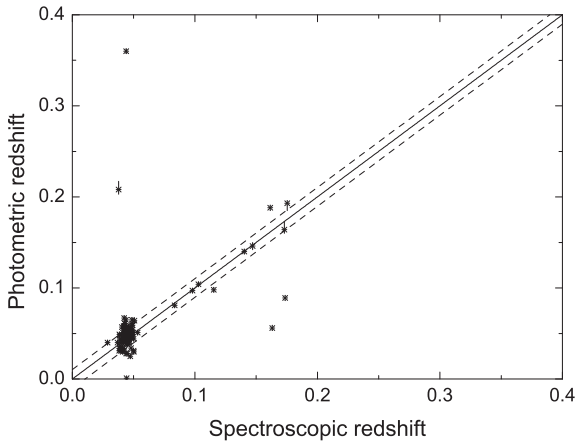

Fig. 5 Comparison between photometric redshift ($z_{\rm ph}$) and spectroscopic redshift ($z_{\rm sp}$) for 157 galaxies brighter than $i_{\rm BATC} = 17.0$ with known spectroscopic redshifts in A119. The solid line corresponds to $z_{\rm sp} = z_{\rm ph}$ and dashed lines indicate an average deviation of 0.0103.

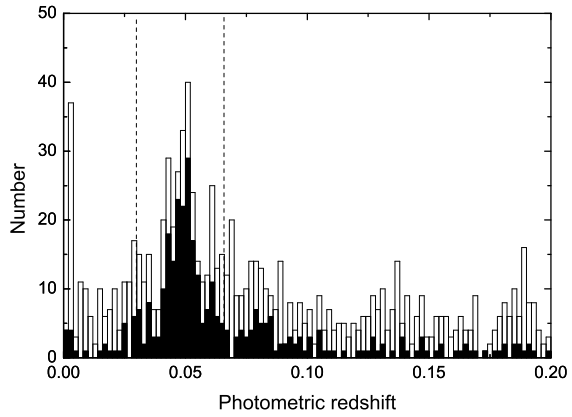

Fig. 6 The distribution of photometric redshifts, with a bin size of 0.002. The black histogram shows $z_{\rm ph}$ of 238 galaxies in sample I. The dashed lines represent the $z_{\rm ph}$ range of the selection criterion.

and three galaxies are found to have more than one counterpart within the searching region, corresponding to a small probability (2.6%) of object blending.

5 PROPERTIES OF THE CLUSTER A119

5.1 Spatial Distribution and Localized Velocity Structure

Based on sample II, we investigate the spatial distribution and localized velocity structure of A119. The left-hand panel of Figure 8 shows contour maps of surface density with a Gaussian smoothing window of $\sigma = 2'$ superimposed on the projected distribution of galaxies in sample II. The early-types and late-types are marked with open circles and asterisks, respectively. The density contour

Table 4 Catalog of 117 Newly-selected Candidates of Member Galaxies in A119

No.	R.A.	Dec.	$z_{\rm ph}$	fracDeV	a	b	c	d	e	f	g	h	i	j	k	m	n	o	p
1	0 57 43.29	−1 30 40.00	0.030	0.080	19.50	20.13	18.84	99.00	19.32	19.49	19.18	19.12	18.66	18.80	18.55	18.80	18.48	18.64	18.52
2	0 56 17.74	−1 19 30.50	0.030	0.000	99.00	21.65	19.15	20.69	20.59	20.24	99.00	21.08	19.48	18.93	20.40	19.60	19.38	20.46	99.00
3	0 54 51.55	−1 13 24.20	0.030	0.376	21.65	21.02	19.58	19.38	18.76	18.66	18.34	18.27	18.11	18.02	17.86	17.85	17.68	17.67	17.88
4	0 56 48.50	−0 54 10.50	0.030	0.474	21.83	21.73	21.07	20.11	20.38	20.24	19.31	19.26	19.19	19.43	19.19	19.22	18.71	19.18	18.26
5	0 57 35.82	−1 23 13.30	0.030	1.000	21.27	19.98	19.44	19.06	18.50	18.47	18.33	18.05	17.75	17.62	17.52	17.49	17.22	17.08	17.59
6	0 58 02.94	−1 27 55.20	0.031	0.504	19.41	19.01	18.74	99.00	18.69	18.44	18.70	99.00	18.28	18.37	18.46	99.00	18.52	18.44	18.26
7	0 57 09.83	−1 11 31.10	0.031	1.000	21.62	20.13	19.84	18.91	19.09	18.79	18.32	18.45	18.11	18.20	18.00	17.84	17.61	17.54	17.36
8	0 56 31.40	−1 33 42.40	0.032	0.082	20.66	19.97	19.51	99.00	18.89	18.80	18.31	18.49	18.13	18.10	18.00	17.89	17.68	17.79	17.65
9	0 55 59.26	−1 16 11.90	0.032	0.000	21.85	20.46	20.60	20.52	20.24	19.73	20.68	19.53	19.30	99.00	19.17	19.45	18.85	18.76	18.53
10	0 56 25.61	−1 10 47.20	0.032	0.333	20.98	20.22	19.73	19.56	18.88	18.86	18.46	18.55	18.28	18.39	18.14	18.19	18.03	17.86	17.53
11	0 55 41.29	−0 56 30.70	0.032	0.358	19.49	18.87	18.62	18.47	18.22	18.23	18.20	18.03	17.81	17.99	17.86	18.00	17.69	17.56	17.45
12	0 56 30.90	−1 09 13.40	0.032	0.295	21.58	20.39	20.09	19.78	19.53	19.28	18.88	18.76	18.59	18.64	18.50	18.45	18.30	18.26	17.69
13	0 56 16.92	−1 32 28.70	0.033	0.384	20.61	19.51	19.23	99.00	18.43	18.35	18.11	17.97	17.88	17.88	17.63	17.59	17.41	17.35	17.73
14	0 55 45.99	−1 24 07.90	0.033	0.417	21.75	20.13	20.33	19.99	19.15	99.00	19.32	18.93	18.60	18.68	18.40	18.44	18.26	18.12	18.42
15	0 57 04.88	−1 10 59.90	0.033	0.275	20.60	19.21	18.73	18.57	17.80	18.00	17.80	17.86	17.67	17.57	17.42	17.41	17.02	17.01	99.00
16	0 55 26.52	−1 37 50.50	0.034	0.000	19.57	19.19	18.52	99.00	18.05	17.98	17.75	17.62	17.54	17.45	17.57	17.39	17.37	17.23	17.43
17	0 56 57.82	−1 33 16.80	0.034	0.011	20.25	19.82	19.08	99.00	18.66	18.45	18.41	18.07	18.07	17.93	17.91	17.84	17.62	17.64	17.68
18	0 56 14.31	−1 15 16.80	0.034	0.972	22.71	99.00	19.49	19.16	18.37	18.22	18.39	17.93	17.66	17.82	17.37	17.26	17.12	16.97	17.31
19	0 56 28.79	−1 20 30.50	0.035	0.179	24.51	20.77	20.23	20.09	19.37	99.00	19.06	19.10	18.61	18.94	18.74	18.55	17.98	18.27	18.50
20	0 56 28.82	−1 36 43.80	0.035	0.000	21.50	20.04	20.44	99.00	19.62	19.70	19.61	19.43	19.11	19.19	19.01	19.22	18.67	18.68	18.47
21	0 55 20.59	−1 12 31.60	0.036	0.154	21.75	20.10	20.10	19.56	19.34	19.06	18.71	18.82	18.55	18.59	99.00	18.51	18.00	17.95	18.60
22	0 55 38.94	−1 09 46.80	0.036	0.030	21.07	21.41	20.31	20.10	19.50	19.43	19.44	18.97	18.99	19.52	99.00	19.09	18.60	18.59	18.50
23	0 56 49.25	−1 01 15.80	0.036	0.076	21.84	20.51	20.21	19.86	19.63	99.00	19.03	19.22	18.74	18.49	18.77	18.56	18.29	18.32	18.30
24	0 57 08.77	−0 56 48.00	0.036	0.393	22.08	21.28	20.20	19.80	19.48	19.46	18.82	18.84	18.67	18.62	18.62	18.72	18.20	18.54	18.45
25	0 55 52.56	−1 21 31.60	0.038	0.725	20.59	20.32	19.40	18.98	18.61	18.52	18.44	17.97	17.89	18.02	17.87	17.65	17.56	17.32	17.95
26	0 57 21.38	−1 16 39.80	0.038	0.129	99.00	22.17	21.12	20.32	20.01	20.05	19.57	19.71	19.48	19.15	19.10	19.23	18.87	18.92	20.79
27	0 55 56.44	−1 36 46.80	0.039	0.209	19.98	19.20	18.61	18.14	17.78	17.69	17.36	17.17	17.06	16.95	16.94	16.79	16.66	16.62	99.00
28	0 55 19.23	−1 16 29.10	0.039	0.000	19.60	18.45	17.84	17.39	16.89	16.85	16.64	16.43	16.23	16.10	16.09	15.85	15.65	15.52	15.50
29	0 55 28.43	−1 41 13.90	0.040	0.274	21.55	20.00	19.52	99.00	18.79	18.66	99.00	18.12	18.05	18.05	17.99	17.78	17.57	17.57	17.69
30	0 55 44.12	−1 29 2.10	0.040	0.248	21.97	21.15	20.34	99.00	19.68	19.32	19.21	18.72	18.80	18.61	18.66	18.52	18.41	18.18	18.76
31	0 55 10.98	−1 04 51.30	0.040	0.157	20.19	19.59	19.36	19.25	19.11	18.94	19.27	18.80	18.90	18.50	19.01	18.81	18.91	18.79	99.00
32	0 56 05.55	−1 03 22.90	0.040	0.489	20.30	19.38	18.64	18.11	17.75	17.57	17.34	17.19	16.98	16.94	16.85	16.69	16.63	16.42	99.00
33	0 56 57.42	−0 57 34.70	0.040	0.370	20.64	19.90	19.33	18.94	18.47	18.37	18.04	17.90	17.72	17.74	17.55	17.50	17.37	17.30	17.03
34	0 55 25.87	−0 57 01.20	0.040	0.950	21.11	20.91	20.09	19.90	19.64	19.18	19.05	18.85	18.68	18.58	99.00	18.61	18.24	18.34	17.83
35	0 55 37.82	−0 56 01.00	0.040	0.000	20.56	19.97	19.76	19.65	18.80	19.08	18.93	18.82	18.85	18.20	99.00	18.38	17.95	17.78	17.99
36	0 55 19.42	−0 48 38.50	0.040	0.094	21.31	21.56	19.85	19.40	19.12	19.02	18.53	18.78	18.56	18.56	99.00	18.53	99.00	18.24	18.07
37	0 56 38.89	−1 00 48.00	0.041	0.986	22.04	99.00	21.49	99.00	21.46	20.29	19.10	19.33	19.44	99.00	19.78	19.14	18.41	18.69	17.57
38	0 55 14.03	−1 04 08.20	0.042	0.317	99.00	20.56	20.32	19.85	19.59	19.40	18.92	18.88	18.69	18.50	99.00	18.12	17.85	17.96	17.72
39	0 57 23.13	−1 43 33.10	0.042	0.502	21.49	20.88	21.09	99.00	19.81	19.91	19.11	19.29	19.41	19.19	18.91	99.00	18.48	18.70	18.32
40	0 54 39.14	−1 36 02.00	0.042	0.589	19.45	19.11	18.39	17.97	17.87	17.81	17.57	17.47	17.35	17.29	17.34	17.21	17.13	17.02	17.09
41	0 55 23.45	−1 17 22.00	0.042	0.578	21.11	21.40	20.34	19.88	19.84	99.00	18.85	19.46	18.80	18.90	19.29	18.88	18.72	18.61	20.00
42	0 58 03.53	−1 40 35.80	0.042	0.000	21.85	99.00	20.64	99.00	20.02	19.84	19.86	99.00	19.23	19.31	19.31	99.00	18.64	19.04	18.93
43	0 55 58.89	−1 17 49.50	0.043	0.000	21.96	20.36	20.32	19.88	19.53	19.36	19.47	19.78	18.86	19.15	19.11	18.73	18.44	18.39	17.78
44	0 55 17.89	−1 17 10.30	0.043	0.631	19.82	19.04	18.22	17.77	17.24	17.12	16.86	16.68	16.49	16.40	16.34	16.19	16.07	15.98	15.96
45	0 56 59.72	−0 51 02.80	0.043	0.246	21.01	20.32	20.33	20.38	19.23	19.46	19.34	19.09	19.16	19.03	18.98	18.87	18.43	18.35	18.65
46	0 55 05.88	−1 39 30.20	0.044	0.259	21.32	20.34	20.32	99.00	19.57	19.81	19.94	19.23	19.28	19.22	19.13	18.91	18.76	18.76	18.23
47	0 55 13.98	−1 07 30.20	0.044	0.441	21.59	20.81	20.12	19.57	19.28	19.09	18.72	18.72	18.55	18.63	18.60	18.43	18.28	18.01	19.91
48	0 56 29.41	−1 11 41.30	0.045	0.139	20.68	20.45	19.71	19.58	18.92	18.90	18.34	18.43	18.25	99.00	18.03	17.92	17.86	17.69	17.59
49	0 56 27.08	−1 20 53.90	0.045	0.898	20.23	19.16	18.63	18.00	17.66	99.00	17.20	17.08	16.86	16.81	99.00	16.55	16.45	16.33	16.26
50	0 54 39.17	−1 34 32.50	0.045	1.000	19.95	19.17	18.45	99.00	17.53	17.48	17.18	17.08	16.84	16.72	16.74	16.53	16.44	16.29	16.46
51	0 56 07.93	−1 00 52.20	0.046	0.350	21.41	20.11	20.22	19.60	19.25	19.14	19.00	18.75	18.45	18.30	18.06	18.03	17.85	17.75	99.00
52	0 55 09.54	−1 03 03.40	0.046	0.000	21.71	22.22	20.03	20.17	18.87	18.98	18.83	18.77	18.54	18.33	18.53	18.25	18.24	18.09	18.42
53	0 55 03.89	−1 22 40.20	0.047	0.586	21.20	20.56	19.73	19.55	18.96	18.89	18.74	18.40	18.22	18.12	18.39	18.07	17.82	17.94	17.87
54	0 56 46.26	−1 36 13.80	0.048	1.000	20.43	19.82	18.94	99.00	18.06	17.90	17.64	17.44	17.31	17.30	17.14	17.06	16.94	16.84	16.73
55	0 55 44.80	−1 34 49.80	0.048	0.933	20.53	19.94	19.09	99.00	18.13	18.02	17.69	17.55	17.42	17.32	17.29	17.08	16.91	16.95	16.80
56	0 55 50.13	−1 28 38.10	0.048	0.000	20.92	20.52	20.13	20.20	19.69	19.78	19.13	18.81	19.25	19.27	19.69	19.15	19.07	19.33	99.00
57	0 55 17.55	−1 16 47.00	0.048	0.336	22.25	21.60	19.81	19.37	18.78	18.63	18.31	18.07	17.77	17.76	17.56	17.37	17.27	17.19	16.96
58	0 56 17.98	−1 15 00.90	0.048	0.000	22.40	21.16	19.87	19.08	18.68	18.49	17.96	18.05	17.79	17.97	17.58	17.39	17.34	17.20	17.94
59	0 56 10.55	−1 04 04.20	0.048	0.283	22.19	99.00	20.36	20.33	19.68	19.50	19.48	19.06	18.78	18.70	18.91	18.72	18.72	18.55	99.00

Table 4 — *Continued.*

No.	R.A.	Dec.	$z_{\rm ph}$	fracDeV	a	b	c	d	e	f	g	h	i	j	k	m	n	o	p
60	0 56 59.41	−1 21 51.50	0.048	0.485	99.00	21.11	20.47	20.28	19.69	19.51	19.73	18.99	18.92	18.86	18.92	18.70	18.90	18.40	19.62
61	0 54 30.41	−1 39 21.10	0.049	0.298	20.91	19.41	18.84	99.00	18.07	17.85	17.54	17.42	17.18	17.14	17.18	16.93	99.00	16.78	16.72
62	0 57 12.41	−0 58 28.50	0.049	0.329	20.92	20.73	19.67	19.12	18.77	18.76	18.36	18.68	18.16	18.16	17.99	17.88	17.67	17.81	99.00
63	0 54 53.93	−1 40 43.10	0.050	0.237	21.08	21.88	20.14	99.00	19.41	19.29	18.83	19.10	18.98	18.73	99.00	18.70	18.51	18.58	18.05
64	0 56 06.48	−1 37 54.00	0.050	0.000	21.01	20.27	19.93	99.00	19.37	19.39	19.58	19.55	19.02	18.94	19.03	18.72	18.82	18.35	17.69
65	0 56 12.34	−1 31 50.20	0.050	0.000	21.12	20.05	19.83	99.00	19.27	19.33	19.23	18.99	18.93	18.86	19.02	18.75	18.77	18.77	19.00
66	0 56 13.87	−1 16 24.30	0.050	0.863	21.99	21.02	20.49	21.37	19.80	19.65	19.84	19.86	18.75	19.18	20.27	18.63	18.48	18.79	18.16
67	0 55 10.34	−1 02 42.90	0.050	0.000	22.14	21.08	20.06	19.73	18.80	18.72	18.43	18.61	18.28	18.07	18.35	17.90	17.80	17.70	18.34
68	0 57 55.99	−0 59 55.80	0.050	0.000	20.19	19.39	18.87	18.64	18.28	18.20	17.95	17.92	17.74	17.59	17.71	17.62	17.50	17.48	17.17
69	0 54 43.20	−1 20 05.10	0.051	0.180	20.40	19.72	19.52	19.08	18.94	99.00	19.10	19.38	18.96	18.88	18.72	18.67	18.58	18.66	17.85
70	0 56 07.58	−1 20 38.10	0.051	1.000	19.72	18.90	18.32	17.83	17.35	17.16	16.91	16.79	16.56	16.55	16.51	16.27	16.19	16.06	16.02
71	0 55 15.35	−0 54 59.90	0.051	0.000	21.42	19.98	19.46	19.11	18.51	18.61	18.23	18.42	18.07	18.06	18.16	17.75	17.65	17.65	17.54
72	0 56 35.20	−1 07 10.90	0.052	0.271	21.61	20.42	20.08	19.97	19.36	19.21	18.82	18.64	18.63	18.38	18.58	18.32	18.21	18.34	18.30
73	0 54 44.56	−1 28 19.30	0.053	0.000	20.29	20.02	19.26	18.68	18.57	18.22	17.88	17.83	17.68	17.60	17.63	17.48	17.28	17.25	17.02
74	0 56 34.55	−1 25 46.20	0.053	0.586	20.67	20.06	19.54	19.10	18.69	18.60	18.07	17.99	18.04	17.84	17.89	17.78	17.84	17.55	17.67
75	0 56 53.33	−1 13 24.70	0.053	0.000	21.79	20.44	20.43	99.00	19.44	19.57	19.12	18.92	19.10	18.85	19.18	18.88	18.73	18.62	18.72
76	0 57 13.58	−1 03 16.30	0.053	0.271	20.23	19.39	18.97	18.67	18.38	18.37	18.16	18.18	18.02	17.98	17.99	17.90	17.73	17.82	18.57
77	0 55 33.50	−1 29 00.80	0.054	0.784	20.49	19.77	19.40	18.91	18.55	18.40	18.09	17.97	17.77	17.69	17.66	17.42	17.27	17.31	17.37
78	0 57 05.14	−0 50 24.90	0.054	0.413	22.61	21.81	20.13	19.99	19.25	19.23	18.74	18.80	18.47	18.50	18.60	99.00	18.26	18.39	17.59
79	0 56 34.49	−0 53 35.80	0.056	0.998	21.03	20.41	20.33	19.73	18.85	18.87	18.70	18.41	18.22	18.15	17.93	17.79	17.71	17.47	17.40
80	0 55 40.63	−1 36 18.20	0.057	0.514	20.88	19.97	19.58	99.00	18.75	18.55	18.20	18.18	18.02	17.98	17.94	17.77	17.68	17.62	99.00
81	0 55 37.21	−1 35 30.30	0.057	0.769	19.89	19.22	18.70	99.00	17.82	17.64	17.40	17.22	17.03	16.91	16.91	16.72	16.65	16.57	16.40
82	0 55 31.75	−1 34 57.60	0.057	0.094	20.82	20.22	19.67	99.00	18.95	18.97	18.64	18.61	18.58	18.38	18.68	18.36	18.36	18.44	18.37
83	0 56 29.31	−1 05 56.50	0.057	0.780	20.36	19.47	19.02	18.45	18.14	18.01	17.75	17.57	17.44	17.54	17.30	17.19	17.10	17.01	16.96
84	0 55 05.80	−0 53 40.30	0.057	0.033	20.32	19.71	19.33	18.63	18.31	18.13	17.85	17.68	17.54	17.47	99.00	17.24	17.14	17.02	17.23
85	0 55 39.07	−1 34 49.90	0.058	1.000	20.97	20.24	19.66	99.00	18.80	18.74	18.43	18.42	18.13	17.97	17.93	17.74	17.69	17.62	17.47
86	0 56 59.62	−1 15 54.20	0.059	0.543	20.41	20.24	19.46	18.96	18.50	18.46	18.09	17.88	17.82	17.90	17.68	17.55	17.42	17.43	17.25
87	0 57 45.14	−1 44 54.00	0.060	0.018	20.77	20.20	19.48	19.02	17.93	18.18	99.00	17.38	17.52	18.24	18.41	18.19	18.84	17.70	17.79
88	0 55 40.59	−1 35 41.10	0.060	0.497	21.08	20.17	20.25	99.00	19.83	19.38	19.45	19.51	19.39	19.39	19.53	19.03	18.98	18.73	17.68
89	0 57 10.97	−1 22 35.70	0.060	0.000	20.30	19.65	19.17	18.87	18.52	18.30	18.09	18.05	17.90	17.95	17.81	17.57	17.70	17.41	17.13
90	0 56 08.43	−1 15 16.00	0.060	0.349	21.20	19.83	19.44	18.80	18.54	18.36	18.24	18.12	17.88	99.00	17.70	17.55	17.54	17.38	17.40
91	0 57 24.61	−0 57 49.10	0.060	0.417	21.44	99.00	20.76	20.34	19.93	19.82	19.45	19.31	19.49	19.45	19.18	19.05	18.83	19.05	21.11
92	0 54 50.51	−0 53 35.50	0.060	0.778	22.49	99.00	21.81	21.57	19.86	20.15	19.44	19.31	19.31	19.40	99.00	18.74	18.79	18.55	17.96
93	0 55 18.68	−0 49 27.20	0.060	0.302	20.22	19.77	19.22	18.72	18.66	18.61	18.49	18.44	18.32	18.43	99.00	18.00	99.00	17.96	18.82
94	0 54 39.05	−0 55 47.10	0.060	0.942	22.30	20.81	22.26	23.47	20.19	20.68	20.86	19.55	19.36	19.90	99.00	19.10	19.07	18.75	17.77
95	0 56 45.13	−1 17 59.80	0.061	0.551	20.07	19.55	18.81	18.37	17.91	17.76	17.47	17.32	17.17	17.17	17.08	16.90	16.81	16.75	16.42
96	0 56 49.00	−1 17 32.90	0.061	0.333	20.19	19.55	18.96	18.30	18.03	17.81	17.40	17.28	17.10	17.03	16.86	16.77	16.69	16.59	16.42
97	0 54 55.40	−1 01 06.80	0.061	0.000	21.62	20.46	20.13	19.91	19.19	19.32	18.85	19.37	19.10	19.21	99.00	18.63	18.69	18.64	18.69
98	0 57 00.21	−0 51 02.70	0.061	0.000	20.34	19.60	19.49	19.05	18.47	18.44	17.88	18.10	17.85	17.86	17.78	17.60	17.61	17.41	17.20
99	0 57 04.09	−1 09 06.60	0.062	0.254	20.34	19.80	19.14	18.78	18.25	18.08	17.81	17.68	17.56	17.38	17.40	17.24	17.23	17.07	17.05
100	0 55 10.65	−0 56 07.90	0.062	0.374	21.51	21.35	19.75	19.65	19.09	19.05	18.99	18.84	18.55	18.75	99.00	18.31	18.52	18.21	18.03
101	0 54 49.28	−0 55 02.20	0.062	0.493	21.50	21.05	20.75	20.31	19.56	19.49	19.33	18.66	18.99	18.91	99.00	18.44	18.65	18.26	18.89
102	0 57 28.06	−1 14 59.00	0.063	0.938	21.68	20.72	20.58	20.05	19.50	19.40	18.98	18.72	18.63	99.00	18.37	18.28	18.02	18.18	17.72
103	0 55 00.15	−1 18 42.90	0.063	0.189	21.35	22.01	20.44	19.81	19.62	99.00	20.31	19.75	19.37	19.21	99.00	18.81	19.60	18.86	18.30
104	0 55 36.59	−0 50 42.80	0.063	0.633	20.35	19.13	18.85	18.42	18.20	18.07	17.98	17.74	17.64	17.57	99.00	17.40	17.43	17.26	17.04
105	0 54 49.48	−1 32 33.90	0.064	0.000	99.00	21.45	19.67	19.62	19.42	19.73	18.68	18.98	19.11	20.30	19.88	18.91	18.16	20.15	99.00
106	0 55 57.48	−1 40 26.10	0.064	0.942	20.13	19.37	18.88	99.00	18.61	18.55	18.43	99.00	18.37	18.53	18.56	18.39	18.43	18.58	19.18
107	0 57 14.62	−1 36 04.40	0.064	0.155	21.03	21.53	20.34	99.00	19.94	20.02	19.94	19.01	19.45	19.70	19.53	19.44	19.28	19.59	19.07
108	0 54 38.22	−1 28 35.00	0.064	0.932	21.28	21.34	20.04	19.91	19.88	19.52	19.76	19.46	19.31	19.20	99.00	19.20	19.04	19.27	18.52
109	0 55 30.97	−1 28 38.20	0.065	0.000	21.20	20.40	19.44	19.18	18.91	18.83	18.31	18.50	18.35	18.30	18.23	18.29	18.23	18.19	18.81
110	0 56 28.27	−0 56 41.20	0.065	1.000	19.47	18.76	18.35	17.95	17.80	17.72	17.47	17.25	17.16	17.17	17.12	16.96	16.93	16.91	16.79
111	0 56 00.93	−0 56 26.80	0.065	0.072	21.54	20.16	20.02	19.50	19.40	19.13	18.57	18.73	18.60	18.57	99.00	18.43	18.35	18.34	18.34
112	0 56 40.83	−0 55 20.40	0.065	0.378	21.59	20.64	20.49	20.11	20.00	19.74	19.58	19.17	19.22	18.95	19.51	18.60	19.25	18.71	17.61
113	0 55 49.02	−0 52 37.10	0.065	0.632	21.41	21.02	20.27	19.85	19.41	19.48	19.33	19.34	19.03	18.92	19.12	18.86	18.69	18.88	18.15
114	0 58 02.90	−1 26 15.70	0.066	0.023	20.27	19.58	19.37	19.13	18.85	18.68	18.45	18.35	18.21	18.15	18.19	99.00	18.01	17.91	17.66
115	0 55 55.93	−1 17 50.20	0.066	0.956	20.51	19.79	19.25	18.72	18.39	18.22	17.83	17.72	17.57	17.62	17.54	17.36	17.38	17.18	17.06
116	0 54 50.14	−0 54 58.70	0.066	0.485	20.94	21.06	20.47	19.86	19.17	18.93	18.71	18.41	18.22	18.07	99.00	17.72	17.76	17.61	17.16
117	0 57 10.32	−0 48 57.60	0.066	0.352	22.41	20.33	20.05	19.71	19.51	19.08	18.60	18.61	18.61	18.39	18.77	99.00	99.00	18.28	20.28

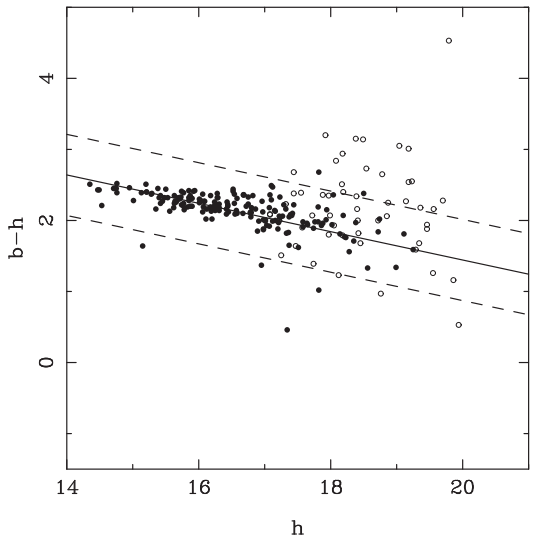

Fig. 7 Color-magnitude relation for early-type galaxies in A119. Early-type member galaxies with known spectroscopic redshifts are denoted by *filled circles*, and newly selected early-type member candidates are denoted by *open circles*. The solid line shows the linear fit for 181 early-type galaxies in sample I. The dashed lines correspond to the intercept denoting the $\pm 3\sigma$ deviation.

for sample II appears to have a more significant deviation from spherical symmetry, indicating that A119 is a complex dynamic system with significant substructures.

Three substructures (A, B and C) shown in Figure 3 are confirmed in Figure 8. The result of the κ-test for sample II is given in Table 3. The probability $P\ (\kappa_n > \kappa_n^{\rm obs})$ is less than 1%, strongly suggesting a more significant detection of substructure. The bubble clustering in clump A appears to be split into two bunches, which makes picture of merging along the line of sight clearer. In addition, two bunches of bubbles are newly detected at about $23'$ southwest and northwest of the main concentration. Considering the large uncertainties of the $z_{\rm ph}$ estimate, follow-up spectroscopy is needed to confirm these two substructures.

5.2 Morphology and Luminosity Segregations

The clustercentric distance R and local galaxy density are traditional parameters tracing the environment in a cluster. Projected local galaxy density is commonly defined as $\Sigma_{10} = 10/(\pi r_{10}^2)$, where r_{10} is the distance from a given galaxy to the ninth nearest neighbor (Dressler 1980). As reviewed by Sandage (2005), morphological classification is the most intuitive tool for extragalactic astronomy. Dressler (1980) investigated the relation between morphology and local galaxy density, the so-called morphology-density relation, and found that the fraction of spiral galaxies decreases with increasing local density for low-redshift galaxy clusters. This relation was subsequently studied by other authors (Hashimoto & Oemler 1999; Goto et al. 2003). Whitmore & Gilmore (1991); Whitmore et al. (1993) re-analyzed the samples of Dressler (1980) and argued that the correlation between morphology and clustercentric radius R appears tighter than the morphology-density relation. Sanroma & Salvador-Sole (1990) and Whitmore et al. (1993) suggested that the global parameter, clustercentric radius R, should be more fundamental. Local and global processes in cluster galaxies are generally considered to be two causes of different morphologies. Due to the close relation between local galaxy density

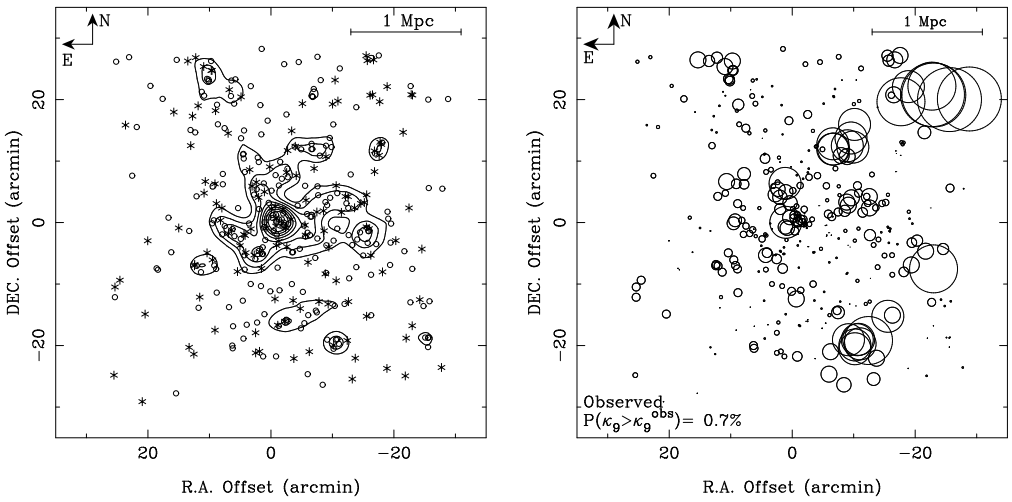

Fig. 8 *Left*: Spatial distribution for 355 member galaxies in sample II. The Gaussian smoothing window is σ=2′; the contour levels are 0.22, 0.32, 0.42, 0.52, 0.62, 0.72, 0.82 and 0.92 arcmin^{-2}. Open circles are early-type galaxies and asterisks are late-type galaxies. *Right*: Bubble plot showing the localized variation for groups of the nine nearest neighbors in sample II.

and clustercentric radius (Beers & Tonry 1986; Merrifield & Kent 1989), the argument about which parameter is more fundamental for morphology and luminosity segregation is still inconclusive.

For checking the presence of luminosity segregation in A119, Pracy et al. (2005) studied the luminosity functions and locations of cluster galaxies in A119 on the basis of their V-band photometry. The information of radial velocities was not taken into account during their sampling. They found that the core radius of a King profile is invariant with intrinsic luminosity. The luminosity functions for member galaxies within three annuli ($r < 0.3$ Mpc, $0.3 < r < 0.6$ Mpc and $0.6 < r < 1.5$ Mpc) are fitted with the Schechter function, and no significant systematic correlation with a cluster-centric radius is found. Alternatively, Driver et al. (1998) defined the dwarf-to-giant ratio (DGR) to quantify the luminosity distribution, and found that giant galaxies are more centrally concentrated than the dwarfs in galaxy clusters. In our paper, because of the limited number of member galaxies, we define the faint-to-bright ratio (FBR) to describe the luminosity distribution: FBR $= \sum N(M_R > -19.5)/\sum N(M_R < -19.5)$, where M_R is the absolute magnitude for the conventional Kron-Cousins R band which can be calculated via the equations in Zhou et al. (2003a).

Figure 9 shows the fraction of late-type galaxies and the FBR as functions of clustercentric radius R and local density Σ_{10} for both samples. For sample I, the late-type galaxy fraction slightly decreases with increasing R, which might be due to the strong bias in sample I. As a matter of fact, the spectroscopic redshifts in sample I are contributed by several observations (see Table 2), and the bright early-type galaxies closer to the cluster center have a greater probability of being selected as spectroscopic targets. A small number of faint member galaxies are spectroscopically detected in the outskirts.

Some faint member galaxies in the low-density outskirts are selected by our multicolor photometry, which results in a prominent increase of the late-type galaxy fraction and the FBR for sample II in the regions with larger R and lower density (see the red points in Fig. 9). The FBR and late-type fraction in sample II appears to increase monotonically with decreasing local density, rather than with increasing clustercentric radius. However, owing to the limited number of member galaxies,

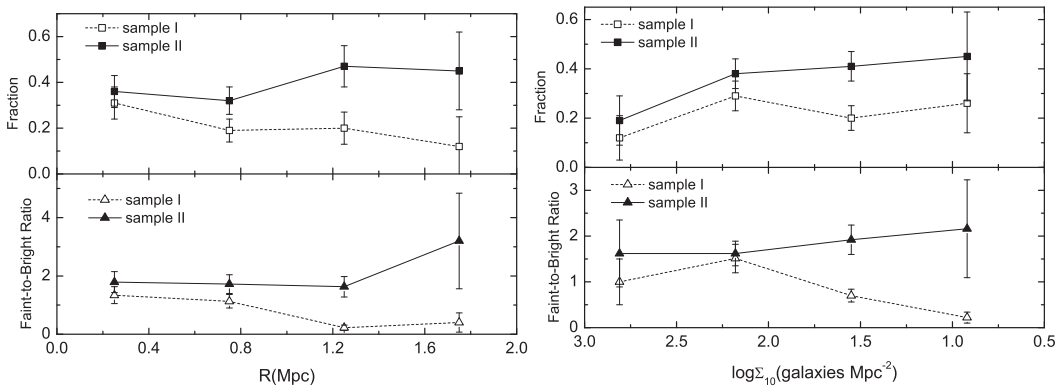

Fig. 9 *Left*: Fraction of late-type galaxies and faint-to-bright ratio (FBR) as functions of cluster-centric radius for sample I and sample II, respectively. *Right*: Fraction of late-type galaxies and FBR as functions of local galaxy density for sample I and sample II, respectively. The width of annuli is 0.5 Mpc, and bin size of local density is $\Delta\log\Sigma_{10} = 0.63$ (galaxies Mpc^{-2}).

significant uncertainties in the late-type galaxy fraction and the FBR can be found for the low-density and outskirt regions in sample II, which will surely reduce the probability of a monotonic increase. Considering the error bars in the right panels of Figure 9, we apply Monte Carlo simulations to estimate the probabilities of a monotonic increase for sample II. As a result, the late-type galaxy fraction has a probability of 31.0% to monotonically increase with the decreasing density, and the probability that the FBR monotonically increases with decreasing density is about 18.8%. Therefore, we may safely conclude that no clear evidence is found for morphology or luminosity segregations in A119. A future study with a deep and complete sample of member galaxies is necessary to further determine which environmental indicator is more fundamental.

6 STAR FORMATION PROPERTIES OF CLUSTER GALAXIES

The star formation properties of member galaxies in a cluster can help us to understand formation and evolution of galaxies and their host cluster. Thus, it is important to observe the systematic tendency of star formation properties for the galaxies in a cluster.

With the evolution synthesis model, PEGASE (version 2.0, Fioc & Rocca-Volmerange 1997, 1999), we investigate the star formation properties of A119. A Salpeter initial mass function (IMF) (Salpeter 1955) is adopted. The star formation rate (SFR) is assumed to have an exponentially decreasing form, $SFR(t) \propto \mathrm{e}^{-t/\tau}$, where the time scale τ ranges from 0.5 to 30.0 Gyr. To avoid the degeneracy between age and metallicity in the model, the same age of 12.7 Gyr is adopted for all the member galaxies in A119, responding to the age of the first generation stars at $z_{\mathrm{c}} = 0.0442$. A zero initial metallicity of the interstellar medium (ISM) is assumed. Firstly, a series of modeled spectra at rest frame ($z = 0$) with various star formation histories are generated by running the PEGASE code. Then we shift them to the observer's frame for a given redshift, and convolve with the transmission functions of the BATC filters. As a result, we obtain the template SED library for the BATC photometric system. Based on the template SED library, the best fit (in the χ^2 sense) to the observed SEDs are performed for 238 member galaxies with known spectrocopic redshifts. The SFR time scale (τ), mean ISM metallicity ($\mathrm{Z_{ISM}}$) and the mean stellar age ($t_\star$) weighted by mass and light for each cluster galaxy can be calculated.

As far we know, early-type galaxies in the field commonly have low star formation rates, whereas late-type galaxies have high star formation activity. This bimodality is modified in dense environ-

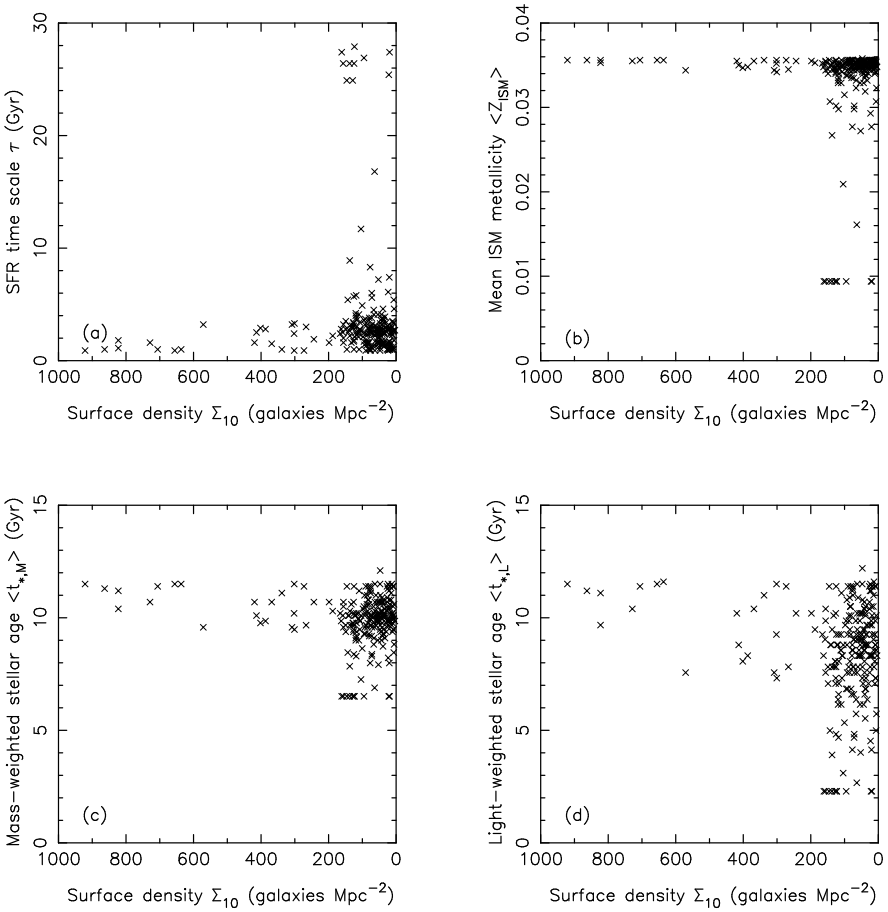

Fig. 10 Star formation properties, such as the SFR time scale τ, mean ISM metallicity and the mean stellar ages weighted by mass and light, for galaxies with known $z_{\rm sp}$ values as functions of local galaxy density.

ments: a higher occurrence of passive spiral galaxies is found in clusters than in the field, whereas star-forming elliptical galaxies are rarer in clusters (Bamford et al. 2009). This suggests that star formation rate couples most strongly to the environment, with morphology being only a secondary correlation. Firstly, we attempt to find the tendency of star formation along the clustercentric radius R of A119. However, no tendencies are found as expected. This suggests that the clustercentric radius is not a good environmental indicator for A119. An alternative explanation is that local processes (e.g., galaxy-scale interaction) affect star formation activities, rather than the global processes (like ram-pressure stripping within the cluster-scale environment). This result again proves the correctness of the morphology-density relation pointed out by Dressler (1980), which can be well explained in the context of the hierarchical cosmological scenario (Poggianti 2004).

Figure 10 shows the star formation properties as a function of the local galaxy density for 238 member galaxies in sample I. We take $\Sigma_{10} = 200\,{\rm Mpc}^{-2}$ as a boundary between the regions with high and low densities. Panel (a) shows that the galaxies in the high-density regions have a shorter SFR time scale than those in the low-density regions. Panel (b) shows that the galaxies in high-

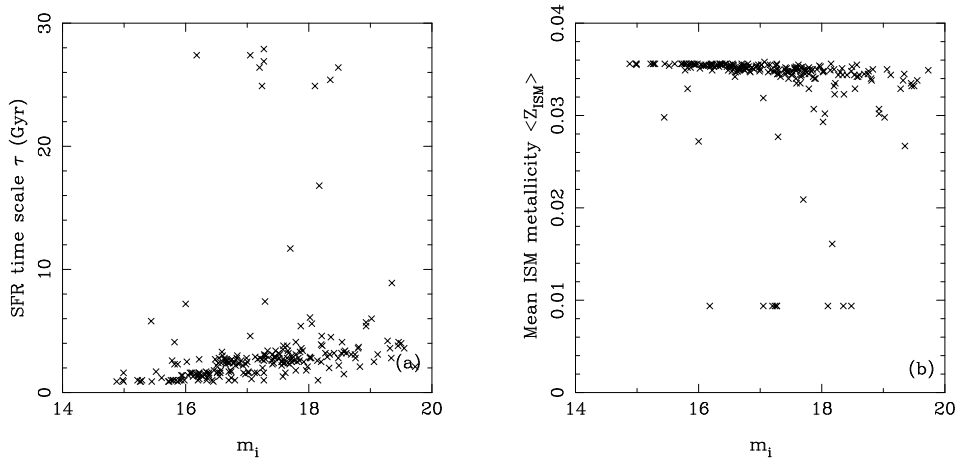

Fig. 11 The SFR time scale τ and mean ISM metallicities for the galaxies with known $z_{\rm sp}$ in A119 plotted against magnitude in the BATC i band.

density regions are more likely to have a higher metallicity in their ISM. It is generally believed that the galaxies in high-density regions (such as the cluster's core) tend to be more luminous and massive. This trend can be commonly interpreted as the luminosity-metallicity relation and the mass-metallicity relation (Garnett & Shields 1987). Panels (c) and (d) show that the galaxies in low-density regions tend to possess a younger stellar population with shorter mean stellar ages weighted by either mass or light. Variation of light-weighted stellar age is remarkably widespread, particularly in the high-density regions, in contrast to mass-weighted stellar age. A possible explanation is that the current SFR in a cluster is mainly contributed by the late-type galaxies in low density regions, and a young stellar population has a greater weight in calculation of the average age. It is reasonable that the light-weighted mean of stellar ages tends to be younger for cluster galaxies.

It is generally considered that member galaxies in a cluster have the same distance modulus; its apparent magnitude could reflect their intrinsic luminosity. The SFR time scale (τ) and mean ISM metallicity for the galaxies in sample I are illustrated in Figure 11, as functions of apparent magnitude in the BATC i band.

Figure 11(a) shows that brighter galaxies tend to have shorter SFR time scales. Massive, luminous member galaxies located in the high-density region began to fall into a gravitational potential well at an earlier time, thus their star formation activities have been reduced by some physical processes for a longer time, which results in a short timescale of star formation.

Figure 11(b) gives the variation of mean ISM metallicities with their magnitudes in the BATC i band. Fainter member galaxies tend to have lower mean ISM metallicities, while luminous galaxies are likely to have greater metallicities. This is consistent with the ideas that metals are selectively lost from faint galaxies with shallow potential wells via galactic winds (Melbourne & Salzer 2002; Tremonti et al. 2004).

7 SUMMARY

X-ray observations suggest that the nearby cluster A119 is not a regular, well-relaxed cluster. We present our multicolor photometry in optical bands for this galaxy cluster, on the basis of the BATC's 15 intermediate filter system that covers almost the whole optical wavelength domain. We obtain the SEDs of 1376 galaxies brighter than $i_{\rm BATC} = 19.5^{\rm m}$ in our field of view of $58' \times 58'$. There are 368

galaxies with available spectroscopic redshifts, among which 238 galaxies with $10\,736\ \mathrm{km\ s^{-1}} < cz_{\rm sp} < 15\,860\ \mathrm{km\ s^{-1}}$ are regarded as member galaxies of A119 (sample I).

Based on sample I, both the projected distribution and the localized velocity structure support the picture that A119 is a dynamically young cluster with some substructures, which is in agreement with the X-ray image. Three potential substructures are confirmed in the localized deviation of the velocity distribution in the central region of A119. Clump A is found to have a very large velocity dispersion, which supports evidence for a merger at the cluster's center along the line of sight. Clump C might be a compact group of galaxies, which have a bulk velocity of $12\,966\ \mathrm{km\ s^{-1}}$.

A photometric redshift technique is applied to the faint galaxies without $z_{\rm sp}$ values, and the CM relation for early-type galaxies is also used to constrain the membership selection. As a result, 117 faint galaxies are selected as candidates of member galaxies. An enlarged sample of 355 member galaxies, called sample II, is obtained by combining with sample I. Based on sample II, projected distribution and localized velocity structure are investigated. The result of the κ-test for sample II definitely suggests significant substructures in A119. The three substructures mentioned above are all enhanced in a bubble plot.

Subsequently, morphology and luminosity segregations on the basis of sample II are investigated. We define the FBR to quantify the luminosity distribution, and find that the fraction of late-type galaxies and the FBR have very small probabilities of showing a monotonic increase with decreasing local galaxy density. No significant evidence for morphology or luminosity segregations is found.

By using the PEGASE evolutionary synthesis model, the star formation properties of sample I are studied. The environmental effect on star formation histories is found for these member galaxies. The bright massive galaxies in the high-density region of A119 are found to be more likely to have shorter SFR time scales, higher mean ISM metallicities and longer mean stellar ages, and vice versa. These results can be well interpreted by the existing correlations, such as the morphology-density relation, the luminosity-metallicity relation and the mass-metallicity relation.

Acknowledgements We thank the anonymous referee for his/her invaluable comments and suggestions. This work was funded by the National Natural Science Foundation of China (Grant Nos. 11173016, 10873016, 11073032, 11003021 and 10803007), and by the National Basic Research Program of China (973 Program; Grant No. 2007CB815403). We would like to thank Profs. Kong, X. and Cheng, F.-Z. at the University of Science and Technology of China for the valuable discussion.

This research has made use of the NED, which is operated by the Jet Propulsion Laboratory, California Institute of Technology, under contract with the National Aeronautics and Space Administration. Funding for the SDSS was provided by the Alfred P. Sloan Foundation, the Participating Institutions, the National Science Foundation, the U.S. Department of Energy, the National Aeronautics and Space Administration, the Japanese Monbukagakusho and the Max Planck Society. The SDSS web site is *http://www.sdss.org*.

References

Abazajian, K., Adelman-McCarthy, J. K., Agüeros, M. A., et al. 2003, AJ, 126, 2081
Abell, G. O. 1958, ApJS, 3, 211
Allen, D. A. 1976, MNRAS, 174, 29P
Arnouts, S., Cristiani, S., Moscardini, L., et al. 1999, MNRAS, 310, 540
Bahcall, N. A. 1988, ARA&A, 26, 631
Bamford, S. P., Nichol, R. C., Baldry, I. K., et al. 2009, MNRAS, 393, 1324
Bautz, L. P., & Morgan, W. W. 1970, ApJ, 162, L149
Beers, T. C., Flynn, K., & Gebhardt, K. 1990, AJ, 100, 32

Beers, T. C., & Tonry, J. L. 1986, ApJ, 300, 557
Bolzonella, M., Miralles, J.-M., & Pelló, R. 2000, A&A, 363, 476
Bower, R. G., Lucey, J. R., & Ellis, R. S. 1992, MNRAS, 254, 601
Brunner, R. J., & Lubin, L. M. 2000, AJ, 120, 2851
Bruzual A., G., & Charlot, S. 1993, ApJ, 405, 538
Buote, D. A., & Tsai, J. C. 1996, ApJ, 458, 27
Cava, A., Bettoni, D., Poggianti, B. M., et al. 2009, A&A, 495, 707
Colless, M., & Dunn, A. M. 1996, ApJ, 458, 435
Cortese, L., Gavazzi, G., Boselli, A., Iglesias-Paramo, J., & Carrasco, L. 2004, A&A, 425, 429
Dale, D. A., Giovanelli, R., Haynes, M. P., et al. 1998, AJ, 115, 418
Dressler, A. 1980, ApJ, 236, 351
Dressler, A., & Shectman, S. A. 1988, AJ, 95, 985
Driver, S. P., Couch, W. J., & Phillipps, S. 1998, MNRAS, 301, 369
Edge, A. C., Stewart, G. C., Fabian, A. C., & Arnaud, K. A. 1990, MNRAS, 245, 559
Fabricant, D., Kurtz, M., Geller, M., et al. 1993, AJ, 105, 788
Fan, X., Burstein, D., Chen, J.-S., et al. 1996, AJ, 112, 628
Feretti, L., Dallacasa, D., Govoni, F., et al. 1999, A&A, 344, 472
Fioc, M., & Rocca-Volmerange, B. 1997, A&A, 326, 950
Fioc, M., & Rocca-Volmerange, B. 1999, A&A, 351, 869
Furusawa, H., Shimasaku, K., Doi, M., & Okamura, S. 2000, ApJ, 534, 624
Garnett, D. R., & Shields, G. A. 1987, ApJ, 317, 82
Geller, M. J., & Beers, T. C. 1982, PASP, 94, 421
Geller, M. J., & Peebles, P. J. E. 1973, ApJ, 184, 329
Girardi, M., Escalera, E., Fadda, D., et al. 1997, ApJ, 482, 41
Goto, T., Yamauchi, C., Fujita, Y., et al. 2003, MNRAS, 346, 601
Gunn, J. E., & Stryker, L. L. 1983, ApJS, 52, 121
Hashimoto, Y., & Oemler, A., Jr. 1999, ApJ, 510, 609
Jones, C., & Forman, W. 1984, ApJ, 276, 38
Katgert, P., Mazure, A., den Hartog, R., et al. 1998, A&AS, 129, 399
Katz, N., & White, S. D. M. 1993, ApJ, 412, 455
Kinman, T. D., & Hintzen, P. 1981, PASP, 93, 405
Lanzetta, K. M., Yahil, A., & Fernández-Soto, A. 1996, Nature, 381, 759
Liu, S.-F., Yuan, Q.-R., Yang, Y.-B., et al. 2011, AJ, 141, 99
Mantz, A., Allen, S. W., Ebeling, H., & Rapetti, D. 2008, MNRAS, 387, 1179
Melbourne, J., & Salzer, J. J. 2002, AJ, 123, 2302
Merrifield, M. R., & Kent, S. M. 1989, AJ, 98, 351
Mohr, J. J., Evrard, A. E., Fabricant, D. G., & Geller, M. J. 1995, ApJ, 447, 8
Oegerle, W. R., & Hill, J. M. 1994, AJ, 107, 857
O'Hara, T. B., Mohr, J. J., Bialek, J. J., & Evrard, A. E. 2006, ApJ, 639, 64
Pan, Z., Yuan, Q., Kong, X., et al. 2012, MNRAS, 421, 36
Pearce, F. R., Thomas, P. A., Couchman, H. M. P., & Edge, A. C. 2000, MNRAS, 317, 1029
Pelló, R., Kneib, J. P., Le Borgne, J. F., et al. 1999, A&A, 346, 359
Peres, C. B., Fabian, A. C., Edge, A. C., et al. 1998, MNRAS, 298, 416
Piffaretti, R., & Valdarnini, R. 2008, A&A, 491, 71
Poggianti, B. 2004, in Proceedings of Baryons in Dark Matter Halos, Novigrad Croatia, 5-9 Oct 2004, eds. R. Dettmar, U. Klein, & P. Salucci (Published by SISSA), 104.1
Postman, M., & Lauer, T. R. 1995, ApJ, 440, 28
Pracy, M. B., Driver, S. P., De Propris, R., Couch, W. J., & Nulsen, P. E. J. 2005, MNRAS, 364, 1147

Rines, K., Geller, M. J., Kurtz, M. J., & Diaferio, A. 2003, AJ, 126, 2152
Saglia, R. P., Burstein, D., Baggley, G., et al. 1997, MNRAS, 292, 499
Salpeter, E. E. 1955, ApJ, 121, 161
Sandage, A. 2005, ARA&A, 43, 581
Sanroma, M., & Salvador-Sole, E. 1990, ApJ, 360, 16
Smith, R. J., Hudson, M. J., Nelan, J. E., et al. 2004, AJ, 128, 1558
Stetson, P. B. 1987, PASP, 99, 191
Tremonti, C. A., Heckman, T. M., Kauffmann, G., et al. 2004, ApJ, 613, 898
Ventimiglia, D. A., Voit, G. M., Donahue, M., & Ameglio, S. 2008, ApJ, 685, 118
Way, M. J., Quintana, H., & Infante, L. 1997, arXiv:astro-ph/9709036
Wegner, G., Colless, M., Saglia, R. P., et al. 1999, MNRAS, 305, 259
West, M. J., Villumsen, J. V., & Dekel, A. 1991, ApJ, 369, 287
Whitmore, B. C., & Gilmore, D. M. 1991, ApJ, 367, 64
Whitmore, B. C., Gilmore, D. M., & Jones, C. 1993, ApJ, 407, 489
Xia, L., Zhou, X., Ma, J., et al. 2002, PASP, 114, 1349
Yahil, A., & Vidal, N. V. 1977, ApJ, 214, 347
Yan, H., Burstein, D., Fan, X., et al. 2000, PASP, 112, 691
Yang, Y., Zhou, X., Yuan, Q., et al. 2004, ApJ, 600, 141
Yuan, Q., Zhou, X., Chen, J., et al. 2001, AJ, 122, 1718
Yuan, Q., Zhou, X., & Jiang, Z. 2003, ApJS, 149, 53
Zhang, Y.-Y., Reiprich, T. H., Finoguenov, A., Hudson, D. S., & Sarazin, C. L. 2009, ApJ, 699, 1178
Zhang, L., Yuan, Q.-R., Zhou, X., et al. 2010, RAA (Research in Astronomy and Astrophysics), 10, 1
Zhou, X., Chen, J., Xu, W., et al. 1999, PASP, 111, 909
Zhou, X., Jiang, Z.-J., Xue, S.-J., et al. 2001, ChJAA (Chin. J. Astron. Astrophys.), 1, 372
Zhou, X., Jiang, Z., Ma, J., et al. 2003a, A&A, 397, 361
Zhou, X., Arimoto, N., Tanaka, I., Jiang, Z., & Chen, J. 2003b, PASJ, 55, 891